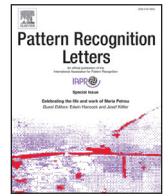




ELSEVIER

Contents lists available at ScienceDirect

# Pattern Recognition Letters

journal homepage: [www.elsevier.com/locate/patrec](http://www.elsevier.com/locate/patrec)

## An efficiency improved recognition algorithm for highly overlapping ellipses: Application to dense bubbly flows

Mathieu de Langlard<sup>a</sup>, Hania Al-Saddik<sup>a</sup>, Sophie Charton<sup>a</sup>, Johan Debayle<sup>b</sup>,  
Fabrice Lamadie<sup>a,\*</sup>

<sup>a</sup>CEA/DEN/DMRC/SA2I, Bagnols-sur-Cèze F-30207, France

<sup>b</sup>Ecole Nationale Supérieure des Mines, SPIN/LGF UMR CNRS 5307, Saint-Étienne, France

### ARTICLE INFO

#### Article history:

Received 17 May 2017

Available online 1 December 2017

#### MSC:

41A05

41A10

65D05

65D17

#### Keywords:

Bubble images

Highly overlapping ellipses

Large ellipse clusters

Sub-clustering approach

### ABSTRACT

Image analysis is a widespread and performant tool for the characterization of particulate systems in chemical engineering. However, for bubbly flows, due to the wide range of particles size, shape and the appearance of large clusters resulting from particles projections overlapping at high hold-up, automatic particle detection remains a challenge. An efficient methodology for bubbly flow characterization based on pattern recognition is presented. The proposed algorithm provides an exhaustive, robust and computationally efficient way of analyzing complex images involving large ellipse clusters even in concentrated medium. The method is fully automated. A sub-clustering approach enables significant computation time reduction. Moreover, thanks to its ease of parallelization, it allows considering real time monitoring.

© 2017 Elsevier B.V. All rights reserved.

### 1. Introduction

Image analysis has become a powerful tool for monitoring particulate systems as the ones encountered in chemical processes, using information extracted from a 2D orthogonal projection of a population of 3D particles [1–3]. The term *particles* is used in this context to designate specifically either bubbles or droplets. Although the experimental part is rather simple and consists of a limited number of set-ups, the image processing methods are many and various. Since the popular Hough transform circle detection [4] and its extension to ellipses detection [5,6], whose application range is usually far from the particulate systems encountered in industrial processes, a lot of studies have been dedicated to the improvement of image processing algorithms. However, the still more or less manual detection of the 2D orthogonal projection of the particles, and the lack of automatic suitable approaches in the case of dense populations, are among the main remaining challenges to be addressed. While promising algorithms are currently emerging to enable fully automatic particle characterization [7,8], robustness issues still arise when large aggregates of 2D projection of particles are involved. These clusters are indeed very dif-

ficult to analyze and specific approaches are necessary. In basic algorithms, these clusters are ignored based on constraint conditions such as sphericity or convexity index. Classical image analysis reasoning does indeed consider that 2D projection of the particles within clusters occurs as a non-selective process and that ignoring these clusters would not bias the measurement. However, large projections of particles are more likely to be present in clusters rather than as individual entities [9]. Thus, ignoring clusters in the measurement would bias the analysis.

There are two major classes of methods for pattern recognition on a 2D image: the non-parametric techniques such as the morphological watershed transform, and the parametric techniques, like the Hough transform or other direct object fitting algorithms. Here, the term *object* refers a 2D bounded set in the Euclidean plane. Lau et al. [10] used the classical watershed transform to determine the particle size distribution (PSD) in dense particle flows. However the objects were assumed to be circular, which is likely to induce a shift of the PSD towards the large particles size and an apparent overestimation of the number of detected particles caused by the processing itself. Still considering the watershed transform, Karn et al. [7] separated the in-focus particles from the out-of-focus ones, which are extracted by using morphological operations, and treated each population independently. This methodology reduces the risk of over-segmentation frequently encoun-

\* Corresponding author.

E-mail addresses: [fabrice.lamadie@cea.fr](mailto:fabrice.lamadie@cea.fr), [lamadie@free.fr](mailto:lamadie@free.fr) (F. Lamadie).

tered with the watershed transform [11]. Farhan et al. [12] used an alternative non-parametric approach. They detected split lines in a clump of 2D convex objects and iterate to refine these split lines using the image intensity. Their technique proved to be efficient and gave satisfactory results in situations where particles touch but do not overlap. While this is the case for the microscopy images of human cells they studied, this situation is rarely encountered in typical chemical engineering applications. Recently, a hybrid approach has been suggested by Fu and Liu [1]. The authors used the benefits of three well known segmentation methods: the watershed transform, the skeleton image and an adaptive threshold [13]. By coupling these techniques, one compensates for the drawbacks of each of the 3 methods used separately for segmentation. Based on several examples of individualization of objects within a cluster, satisfactory agreement was additionally assessed by the authors. Many examples of parametric processing methods applied to the detection of particles projections are also related in the literature. For their study of emulsification kinetics, Khalil et al. [14] assumed that the droplets were spherical and they investigated the time-evolution of the PSD using the famous Hough transform developed by Illingworth and Kittler [4]. However, this method failed when too many projections of particles overlap, even if the generalized Hough transform is used. For their study of bubbly flows, Honkanen et al. [15] proposed an original algorithm to detect overlapping ellipses corresponding to the 2D orthogonal projections of ellipsoidal bubbles in a dense population. In this approach, the boundary of the particles cluster is first detected. Then the points of the boundary that represent the connecting points of overlapping objects (subsequently referred to as concavity points) are found. The sections of the edge delimited by the connecting points and belonging to the same object are grouped. At last an ellipse is fitted on each cluster of edge segments. However, the method used for grouping the edge segments is not fully robust and often leads to incorrect detection even in the case of small clumps of objects. More recently, an improved method was proposed by Zhang et al. [16]. It consists of grouping the segments according to an average distance deviation criterion (called ADD) between the fitted ellipse, on one hand, and the corresponding group of segments in the image on the other hand. However, instead of solving the global minimization problem according to the merit function ADD, the authors proposed to group the segments according to 3 constraints. While the technique described by Zhang et al. [16] provides a significant improvement for the detection of ellipses in a clump of objects (e.g. compared to Honkanen et al. [15] and Shen et al. [17]), the constraints imposed are empirical and must be adjusted for each new configuration of overlapping ellipses. An alternative approach based on seed points extraction and fast radial symmetry transform has been recently proposed by Zafari et al. [18] for the segmentation of overlapping elliptical objects in poor quality images. Although the method is robust and fast, it is strongly dependent on the performance of the seed points extraction.

Hence, among the available image processing techniques, none of them are really suitable for fast and/or efficient detection of overlapping, and possibly non-spherical particles, such as the ones prevailing in images typical of the dense bubbly flow encounters in many industrial applications. In this study, using the ADD criteria brought out by Zhang et al. [16], we describe a fully automated method for grouping the edge segments which is both efficient in terms of ellipses detection, and from a computational point of view, by offering interesting parallelization potential to speed-up the calculation, thus enabling online monitoring.

## 2. The proposed method

In this section, the main steps to achieve ellipse cluster decomposition in a binary image are described. The prior transforma-

tion of gray level images into suitable binary images is treated in Section 3.2. Starting from a binary image, the pattern recognition process consists of the following successive steps: i) identification of all the Region of Interest (RoI) - note that a RoI can be an isolated ellipse as well as a cluster of ellipses -, ii) extraction of the edge of the whole RoI, iii) splitting the edge into segments separated by connecting points, iv) grouping the segments, v) fitting an ellipse on each group of segment, vi) candidate ellipses evaluation and bad candidates rejection.

### 2.1. Detection of edge segments

Identification of RoI in a 2D binary image and subsequent contour extraction is classical in image processing, and will not be detailed further [19]. Segment detection along the contour is achieved through the detection of what is called "connecting points" [15], i.e. the positions of local minima of the curvature function along the boundary. The curvature of a 2D set boundary exists if the arc boundary of the regarded set is twice differentiable with continuous second derivative. Methods to compute the curvature of a boundary set on a 2D image can be found in [20]. These connecting points can therefore be interpreted as concavity points, which will be used by the detection algorithm.

Here, the detection method proposed by Farhan et al. [12] is used. A straight line segment of user-defined length connecting two points of the contour is moved along the boundary. As long as the straight line segment is totally enclosed in the cluster (in green in Fig. 1), the convexity of the boundary between the two contour points is guaranteed. Otherwise (in red in Fig. 1), there exists at least one concavity point in this particular part of the contour. The exact location corresponds to the maximum of the Euclidean distance between the considered contour segment and the probe line. Then, only one concavity point can be detected when the convexity condition is violated. The process, illustrated in Fig. 1a, is repeated until the boundary is totally swept. Note that the length of the straight line segment has to be adapted in order to minimize the number of missed concavity points, as shown in Fig. 1b.

Practically speaking, the construction of the line segment is as followed. Pick up a pixel of the contour. The line joining this pixel and the one of the contour located at 25 pixels away is the straight line segment. In this way, its length is changing depending on the curvature of the arc of the contour that defines it. This construction is robust as it can fit to the shape of any cluster of objects. It has been observed through experiments that such a distance - fixed here at 25 - between the extremities of the line segment gives satisfactory results. Moreover, slightly changing this value (e.g.  $\pm 10$  pixels) does not really affect the detection of the concavity points. There are two ways of defining the step size when the straight line segment is moved along the contour. If the convexity criterion is satisfied, the third adjacent point to the previous *first* extremity of the straight line segment is taken as the initial point. Otherwise, the third adjacent point to the previous *second* extremity of the line segment is chosen.

Following the detection of concavity points, the contour is divided into  $n$  segments (where  $n$  is the number of concavity points). Each segment is assumed to belong to at least one ellipse embedded in the cluster, and an ellipse can potentially include several segments. As a consequence, it is mandatory to find the best combination of the  $n$  segments into  $p$  ellipses in order to extract the most probable cluster decomposition. It is worth noting that other methods for detecting these concavity points have been proposed in the literature such as the detection of local minima in the curvature function [15,20,21], a breakpoints detection by rotating curve [17] or a polygonal approximation technique used by Zhang et al. [16]. The technique adopted in this paper has the merit to be fast, robust and easy to implement.

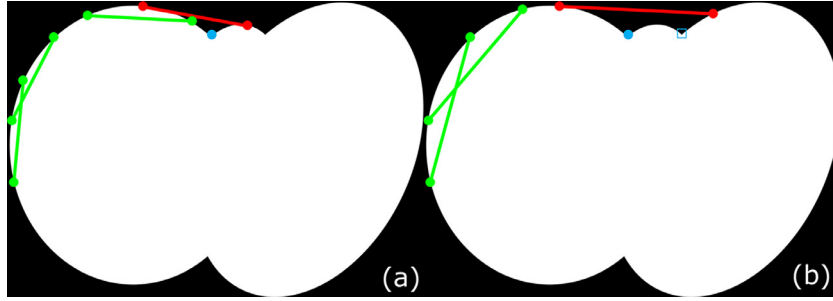


**Fig. 1.** Illustration of the method of concavity points detection - (a) Detection of a concavity point (marked with a plain blue circle) (b) Situation where a concavity point is missed (marked with an open blue square). (For interpretation of the references to color in this figure legend, the reader is referred to the web version of this article.)

In order to improve the efficiency of the algorithm, the area of the convex hull,  $A_{CH}$ , of clusters exhibiting a single concavity point is calculated, and compared to the area,  $A$ , of the considered cluster using the following ratio:

$$cvx = \frac{A}{A_{CH}} \quad (1)$$

This merit function,  $cvx$ , is directly connected to the convexity of the cluster. By comparing  $cvx$  with a given threshold (here 0.95) it becomes possible to discriminate a single ellipse from clusters of two ellipses with a single concavity point. When a cluster of two ellipses is detected then a second connecting point is added in front of the first one. This additional process reduces fitting errors.

## 2.2. Segment association and ellipse selection

The next step addresses segment combination and ellipse fitting. As discussed in introduction, several grouping methods have been evaluated in the literature [15–17,20]. They generally suffer either from bad recognition, as in the case of large cluster of particles, or from robustness issues, as in the case of highly noisy images or from relatively high computing time requirements. The proposed method, called Global Segments Combinations (GSC), is based on an exhaustive enumeration of all possible combinations of segments, followed by a selection of the best combination thanks to a merit function, and is aimed at addressing these weaknesses.

The Stirling partition numbers (also called Stirling number of the second kind) are particularly convenient to perform this enumeration task. Indeed, in combinatorics, the Stirling partition number  $P(n, p)$  designates the number of possible ways to partition a set of  $n$  objects into  $p$  non-empty subsets. For any value of  $n$  and  $p$ ,  $P(n, p)$  can be calculated according to the following expression:

$$P(n, p) = \frac{1}{p!} \sum_{\substack{n_1 + \dots + n_p = n \\ n_i > 0}} \frac{n!}{n_1! \dots n_p!} \quad (2)$$

Once all combinations have been identified in a cluster or a sub-cluster, the segments are grouped according to these different enumerated combinations, and an ellipse is fitted for each obtained portions of contour. For instance, in the simple case  $n = 3$ , there are 5 different ways of grouping the segments: i) 3 ellipses are generated to fit the single combination of the 3 “groups” of individual segments in  $P(3, 3)$ , ii) 2 candidate ellipses are considered for each of the 3 possible combinations of 2 groups of segments (e.g. 1 individual segment and 1 pair of segments), within  $P(3, 2)$ , iii) at last one single ellipse is treated in  $P(3, 1)$ , that accounts for the single combination gathering the all 3 segments in the same group.

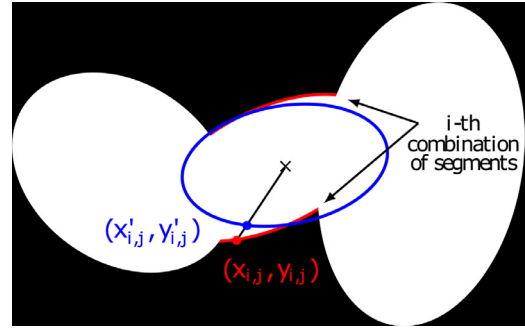


**Fig. 2.** The  $i$ -th combination (in red) is matched with an ellipse (in blue). For each point  $j$  of the  $i$ -th combination  $(x_{i,j}, y_{i,j})$  the distance to the corresponding point of the fitted ellipse  $(x'_{i,j}, y'_{i,j})$  is calculated. (For interpretation of the references to color in this figure legend, the reader is referred to the web version of this article.)

The direct least-square fitting algorithm developed by Fitzgibbon et al. [22] is used to assess the quality of the ellipse fitting in terms of the *Average Distance Deviation (ADD)* between the candidate ellipses and the corresponding contour position. Denoting  $m$  the number of pixels in the considered group of segments, and considering the  $i$ -th group of segments within a set of combinations including  $k$  groups of segments, it reads in Cartesian coordinates:

$$ADD_i = \frac{1}{m^i} \sum_{j=1}^{m^i} \sqrt{(x_{i,j} - x'_{i,j})^2 + (y_{i,j} - y'_{i,j})^2} \quad (3)$$

where  $m^i$  is the number of pixels of the  $i$ -th group of segments,  $(x_{i,j}, y_{i,j})$  are the Cartesian coordinates of pixel  $j$  belonging to the  $i$ -th group of segments,  $(x'_{i,j}, y'_{i,j})$  are the Cartesian coordinates of the corresponding point  $j$  of the ellipse fitted to the  $i$ -th group of segments. This point is defined as the intersection between the fitted ellipse and the line going through both its center and the point of coordinates  $(x_{i,j}, y_{i,j})$ , see Fig. 2.

The notion of distance adopted for expressing  $ADD_i$  can be conveniently reformulated as follow:

$$ADD_i = \frac{1}{m^i} \sum_{j=1}^{m^i} \left( 1 - \frac{1}{\left| \frac{x_{i,j}^2}{a_i^2} + \frac{y_{i,j}^2}{b_i^2} \right|} \right) \quad (4)$$

where  $a_i$  and  $b_i$  denotes the two semi-axis of the ellipse  $i$ . Compared to Eq. (3), Eq. (4) involves only known parameters. It can be evaluated from simple trigonometric calculations. Finally the total average distance deviation  $ADD_{tot}$ , used as the merit function of the considered combination, is obtained by summing the  $ADD_i$  of the

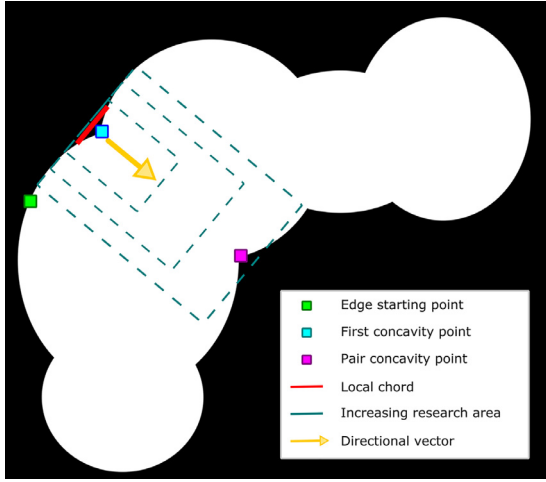


**Fig. 3.** Schematic illustration of a concavity point-pair matching on a cluster. (For interpretation of the references to color in the text, the reader is referred to the web version of this article.)

$k$  contributing groups of segments in the combination:

$$ADD_{tot} = \sum_{i=1}^k ADD_i \quad (5)$$

The combination that exhibits the smallest total average distance deviation  $ADD_{tot}$  among the  $P_n$  possible combinations (corresponding to the Bell numbers) is retained as the solution.

### 2.3. Large cluster decomposition

As previously discussed, the evaluation of all combinations is possible only if the number of segments remains limited. Otherwise, the cluster must be subdivided. The main idea of the decomposition technique is to find appropriate split lines to divide the cluster. A split line is a line which passes through a pair of concavity points and separates the element into sub-clusters of reasonable size, *i.e.* including less than 8 or 9 segments. Additionally, a minimum number of segments (4 or 5) is imposed in order to prevent the separation of segments involved in the same ellipse. As an example, a cluster of 24 segments will be divided into 3 sub-clusters of about 7–9 segments while a cluster of 23 segments will be divided in 2 sub-clusters of 7–9 segments and one sub-cluster of 5–7 segments. Note that these parameters are determined considering the processing time and not adjusted for each image. The detection of split lines is an iterative process based on the work of Farhan et al. [12]. It is depicted on Fig. 3. Starting from a concavity point, a local chord (in red in Fig. 3) is extracted and a directional vector (in yellow), orthogonal to the local chord, is calculated. A rectangular area which starts from the local chord and following the direction of the vector is constructed, the size of which is iteratively increased until including another concavity point. This second point is then linked to the first concavity point to define a split line. Using this split line, the cluster is divided in two sub-clusters and the number of segments included in each sub-clusters is evaluated. If one of the two sub-clusters matches the size condition, the split line is retained. Otherwise, the entire process is repeated starting from the next concavity point in the contour.

The whole process, *i.e.* cluster decomposition and ellipse fitting, is illustrated in Fig. 4, in the case of a 17 segments cluster. In this example, the initial cluster is decomposed into three sub-clusters of 5, 4 and 8 segments respectively. The total number of combinations, initially equal to  $8.28 \times 10^{11}$  is subsequently reduced to  $P_5 + P_4 + P_8 = 4207$ , thus highlighting the relevance of the de-

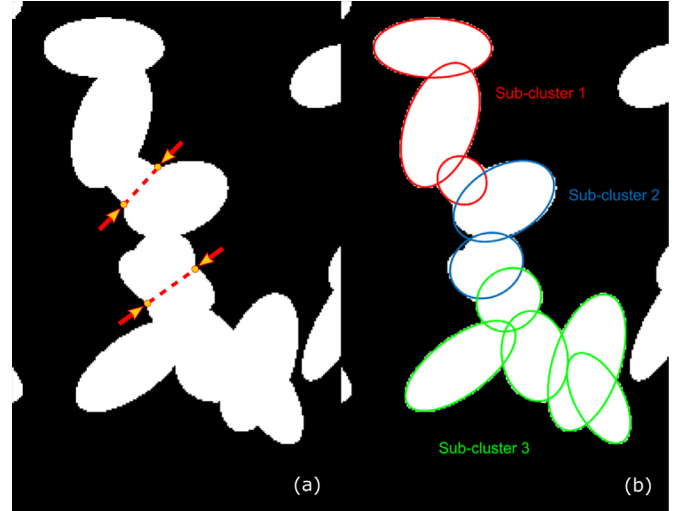


**Fig. 4.** Illustration of cluster decomposition and ellipse fitting in the case of a cluster involving 17 segments - (a) Initial cluster and detected split - (b) resulting sub-clusters and ellipse fitting. (For interpretation of the references to color in this figure legend, the reader is referred to the web version of this article.)

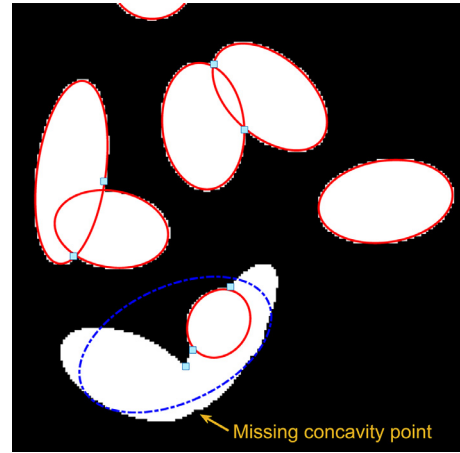


**Fig. 5.** Example of a missing connecting point due to a smooth overlapping of ellipses. The blue ellipse is due to a bad segment association. (For interpretation of the references to color in this figure legend, the reader is referred to the web version of this article.)

composition. Sub-clustering moreover provides a high potential of parallelization to the algorithm. Indeed, the GSC algorithm can be processed independently on each sub-cluster, and the final result is obtained by a simple concatenation of each sub-cluster solution.

### 2.4. Ellipses checking and bad fitting rejection

The algorithm is strongly dependent on the connecting points detection. Missing a connecting point can occur during the detection process, for instance in strongly overlapping configurations. This may induce incorrect segment associations and therefore false ellipse fitting, as illustrated in Fig. 5, where the 3 overlapping ellipses in the cluster at the bottom of the image are modeled by two unsuitable objects. To minimize the impact of this kind of errors, a final test is performed on each detected candidate. A mask, corresponding to the considered ellipse is constructed and used to detect the pixels embedded in the ellipse, in the binary image. If the number of pixels with a 0 value is smaller than a given criterion (typically 10% of the total number of pixels), the candidate ellipse is retained, otherwise it is rejected.

**Table 1**

Performances of the 3 tested methods, including the proposed GSC, for highly dense ellipses population images (50 images of approx. 200 objects each).

Algorithm	TPR	PPV	JSC
Zafari et al. [24]	0.84	0.85	0.79
Park et al. [23]	0.67	0.87	0.71
Proposed method	0.87	0.95	0.91

### 3. Results and discussion

#### 3.1. Performance evaluation on synthetic images

The algorithms performance was first assessed using synthetic images. Indeed, the number of objects involved in a synthetic image is perfectly known and each object is fully characterized, which is usually not the case for "real" images. To this aim, a set of 50 synthetic images of 150–200 overlapping elliptical objects was considered. For the 9000 ellipses in the test case the semi-minor axis, denoted  $a$ , follows a uniform law in the interval [10, 20] pixels, and the semi-major axis, denoted  $b$ , follows a uniform law in the interval [15, 40] pixels. They cover, on average,  $22.19\% \pm 0.36\%$  of the total image surface, which is a typical value encountered in bubbles or droplets flows. Here, no constraint has been imposed on the overlapping ratio: ellipses can completely cover each other.

The proposed method, *i.e.* the GSC algorithm combined with the sub-clustering approach, was compared to two techniques pulled from the state of the art, whose codes are available online, and that are adapted to the detection of clustered ellipses: the method proposed by Park et al. [23] based on a classification and the one proposed by Zafari et al. [24] based on ellipses fitting. For comparison purposes, three usual quantitative performance metrics were used: the Jaccard Similarity Coefficient (JSC), the True positive Rate (TPR) and the Positive Predictive Value (PPV). The TPR and PPV are defined as followed

$$TPR = \frac{TP}{TP + FN} \quad (6)$$

$$PPV = \frac{TP}{TP + FP} \quad (7)$$

where TP (True Positive) is the number of correctly segmented ellipses, FN (False Negative) is the number of missed ellipses and FP (False Positive) is the number of incorrectly segmented ellipses. The TPR can be interpreted as the conditional probability of detecting an ellipse given that the ellipse is indeed correct, while the PPV corresponds to the probability that a segmented ellipses is a correct ellipse. The JSC provides a more quantitative measurement of the quality of the segmentation process. Starting from a binary image of the segmented ellipse  $E_s$ , the JSC is computed with the following expression:

$$JSC = \frac{E_s \cap E_t}{E_s \cup E_t} \quad (8)$$

where  $E_t$  is the binary map of the true ellipse. The JSC requires a threshold value. Following [24] recommendations, we fixed it to 0.5. Given an image, the JSC are generally averaged in order to form a new metric, the AJSC (average JSC) which measures the mean segmentation performance in the image. The statistics obtained on the same computer with the three competing methods for the set of 50 synthetic images considered here are summarized in Table 1. Note that for the 2 literature methods, the adjustable parameters were set to the values recommended by the authors. As evidenced by Table 1, the GSC method outperforms the 2 other methods regardless of the considered metrics. Otherwise, CPU processing times are equivalent for the 3 methods, and revealed to be

**Table 2**

Compared features of the particles populations.

Criteria	Actual population	Measured population
Number of objects	9216	8750
Max $D_{eq}$	56.3 px	88.9 px
Min $D_{eq}$	24.6 px	5.7 px
Mean $D_{eq}$	40.0 px	40.1 px
Variance $D_{eq}$	6.7 px	8.4 px

low compared to conventional methods used for multiphase flow applications, that are not able to handle large clusters.

For the sake of illustration, the results obtained on a single image are compared in Fig. 6 (blue stands for real data, red for GSC, green for Zafari et al. [24] and magenta for Park et al. [23]). The GSC method was further tested on the whole set of images considering the equivalent diameter, a more relevant metric for multiphase flow characterization. The equivalent diameter,  $D_{eq}$ , is defined as the diameter of the disk with the same area as the ellipse:  $D_{eq} = 2\sqrt{ab}$ . More than 95% of the ellipses are detected by the GSC method. Two tails are however exhibited in the distribution returned by the algorithm (Fig. 7). They stand for particles that are out of the range of diameters in the image and whose size is either underestimated (on the left-hand side) or overestimated (on the right-hand side) by the algorithm. Each tail represents respectively 2.0 and 2.5% of the detected objects, which is nevertheless a satisfactory result since at least 90% of the ellipses are correctly measured by the model. An excellent agreement is also achieved regarding the two first moments of the distribution (see Table 2), that are usual indicators of bubbly flow systems. Moreover, this good agreement is also consistent with the morphological features of the dispersed phase. For instance, the comparison of the ellipticity information of the numerical target and the one returned by the algorithm shows that more of 91% of the results are strictly included in the target range.

To highlight the benefit of the post-processing procedure, the detection of ellipses was repeated without the post-processing. The resulting distribution is plot in red in Fig. 7. It can be observed that the post-processing strongly reduces the number of wrong detected ellipses of a larger size. Thus, while the first moment of the distribution does not change that much (41.2 px), the standard deviation is much higher when no post-processing is used (9.7 px compared to 8.4 px). Consequently, the error on the standard deviation is more important if the post-processing procedure is not used (44.8%).

#### 3.2. Application to real bubbly flow images

Besides the good results achieved on synthetic images, the performances of the proposed GSC method have been investigated on a set of experimental gas-liquid flow images.

The flow takes place in a glass cylinder (height 250 mm, diameter 100 mm) provided at mid-height with two opposite planar optical windows in order to minimize light distortions. The tank is filled with deionized water, and air is injected at the bottom through a sintered glass disk (with pore size in the range 40–90 nm). Due to buoyancy, bubbles are rising in the liquids, pass in front of the windows and freely escape the cylinder at the top. Three gas flow-rates have been tested in order to generate different size and concentration of bubbles ( $Q = 5, 10, 50$  L/h).

The optical setup consists in a green collimated light-source, a bi-telecentric lens (magnification  $\times 17.2$   $\mu\text{m}/\text{pixel}$ ) and a high resolution and high dynamic CMOS camera (1.1 MPixel, 12 bits). Acquisitions are conducted at 50 fps, with an exposure time of 1/60,000 s in order to "freeze" the bubble's motion. Such a configuration, associating bi-telecentric lens and collimated light, is

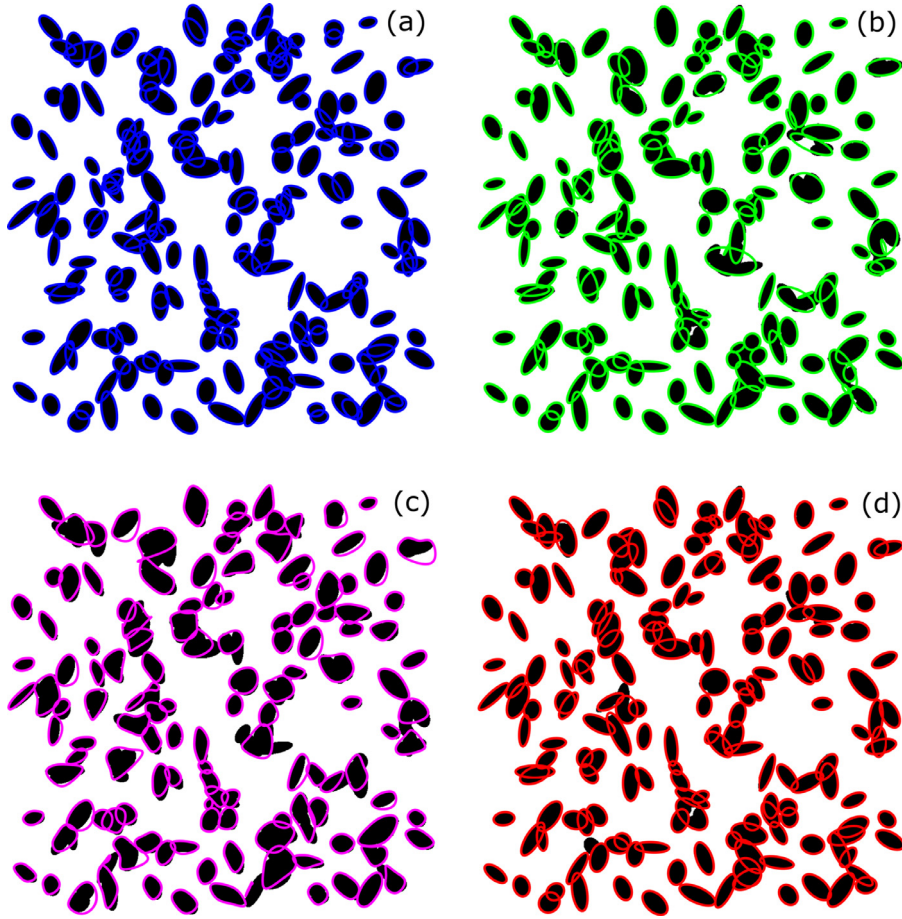


**Fig. 6.** Example of segmentation results on a synthetic image including 200 ellipses: (a) real data, (b) Zafari et al. [24], (c) Park et al. [23], and (d) GSC. (For interpretation of the references to color in this figure legend, the reader is referred to the web version of this article.)

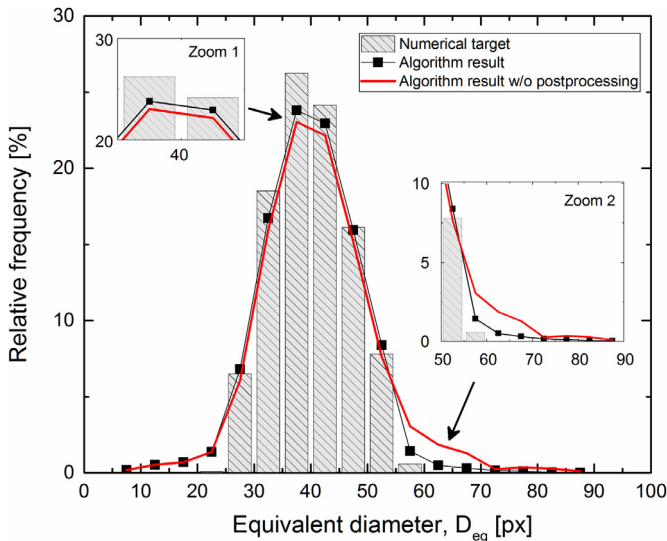


**Fig. 7.** Comparison of the relative frequency of equivalent diameter between the numerical target and the proposed algorithm results (with and without post-processing).

particularly suitable for two-phase flow observation as it provides high contrast images. Indeed, due to the bi-telecentricity, the sensor records a shadow which strictly corresponds to the object’s projected area, and the local contrast between the particles and

the image’s background is generally excellent (more than 20 considering the Weber’s contrast and a 8 bits image).

Although the exact number and the features of the particles are not known in this case, this test enables the code robustness on real images to be assessed, e.g. images subjected to light heterogeneity, noise, and other biases. The surface concentration of bubbles has been evaluated from bubble density measurements in the 2D images, to respectively:  $35.1\% \pm 3.2\%$ ,  $37.9.1\% \pm 3.2\%$  and  $47.9\% \pm 5.1\%$ . Note that the surface concentration is not representative of the actual gas hold-up in the equipment. Moreover, according to Clift et al. [25] the formation of ellipsoidal bubbles is promoted under the considered operating conditions.

A pre-processing procedure, that aims to binarize the recorded gray-level images, is applied in order to extract the edge of each cluster or isolated particles. It consists of four main steps: i) mean image calculation and subtraction from each original image in the dataset, in order to achieve a more uniform background, ii) enhancement of the contrast by applying a top-hat and a bottom-hat filter, iii) noise removal using a median filter, and iv) application of an automated local thresholding [26]. Some cleaning operations are also performed to fill the holes and to remove the very small particles (less than few pixels) by morphological opening with a disk-shape structuring element. At last, the particles or clusters touching the image borders, and therefore not totally displayed, are removed.

The GSC method has been applied to identify the different particles on the experimental images. The result of the ellipse fitting procedure is illustrated in Fig. 8. This typical image exhibits a high

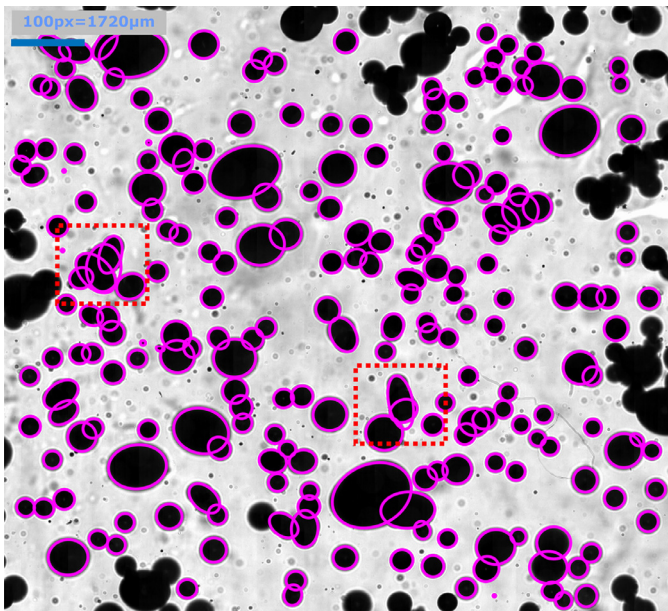


**Fig. 8.** Performances of the proposed algorithm on an experimental acquisition. ( $Q = 10$  L/h). 181 ellipses have been detected. The red boxes highlight the two bad fits. Note that clusters touching the border are not considered. (For interpretation of the references to color in this figure legend, the reader is referred to the web version of this article.)

proportion of clusters, and highlights the non-sphericity of most bubbles, that justifies the need for an algorithm capable of handling these features.

The agreement between the detected ellipses (in pink) and the bubble edges is very good, with only 2 bad fittings *versus* 181 correct detections, thus attesting the algorithm efficiency on real images. Usually three cases of bad ellipse detection are observed. The first one is obviously when the bubbles do not exhibit an ellipse shape but more likely a caps shape. In this case, although an ellipse is fitted on the contour, the latter is rejected by the bad fitting rejection process. The second case occurs for clusters with a very complex shape, for which some concavity points are not detected. Again, the wrong candidate ellipses are not retained by the rejection method described in Section 2.4. The third issue concerns out-of-focus bubbles that exhibit blurred contours. The restoration of out-of-focus particles has already been addressed by Presles et al. [27]. This methodology can be used here, for instance using the Sum-of-Modified Laplacian to detect the out-of-focus particles [28].

Using this technique, process evolutions can efficiently be monitored. Thereby, Fig. 9 compares the evolution of the equivalent diameter for increasing gas flow-rate values. It has to be emphasized that the detection is not made for clusters of objects that hit the edges of the observation window. Thus, some edge effects appear that introduce a bias for the computation of the density number of objects [29] or for the estimation of size distribution [9]. This issue can be handled by taking a sub-image (a reference window) of the observation window where only detected particles are observable. Then, only particles whose centroid belongs to this reference window are taken into consideration. This sampling rule is called the Miles' associated point rule [30]. Alternatively, the Gundersen's tiling rule can also be applied [31]. These techniques are classical methods in the field of stereology to derive unbiased estimators [29].

The physical behavior of the system is quite well captured by the optical chain and the image processing method. While a narrow PSD is observed at moderate flow-rate ( $Q = 5$  L/h), the lat-

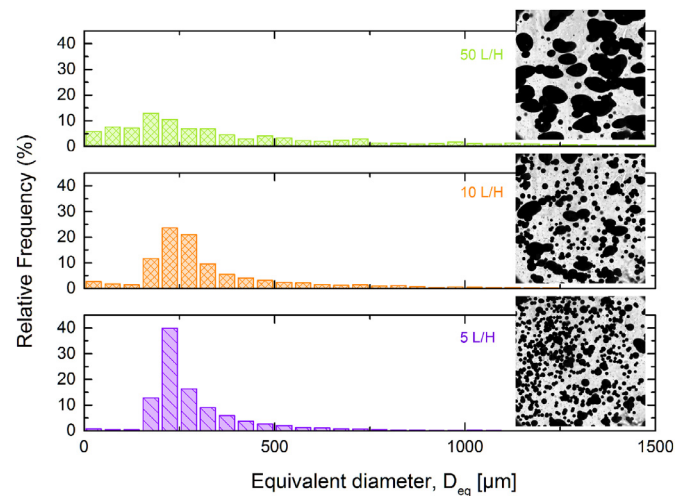


**Fig. 9.** Evolution of the relative frequency of equivalent diameter with the gas flow-rate obtained from the analysis of 50 images (more than 4000 bubbles per case).

ter broadens as the flow-rate increases due to more coalescence events (most of them were observed to occur at the sparger's surface). Increasing the flow-rate moreover results in an increase of the proportion of clusters in the image (as evidenced by the inserts in Fig. 9).

#### 4. Summary and conclusion

This paper presents a complete method for recognizing highly overlapping ellipses. Thanks to the GSC algorithm and the sub-clustering process, the proposed method provides an exhaustive, robust and computationally efficient ellipse recognition algorithm in large clusters. Its performances have been assessed on synthetic images, which enabled to compare the distributions of the equivalent diameter of the detected and generated objects. Even if an exhaustive enumeration could be seen as a naive approach at first, it turns out to be a powerful method for dealing with larger clusters when it is combined with the decomposition procedure proposed. Optimizing the grouping process on a limited search space, as it is usually done in the literature, leads to a lack of robustness and of accuracy. The comparison in Section 3 with two other existing methods using a segment grouping approach has highlighted significant improvements: 95% of the segmented ellipses were correct for the proposed algorithm compared to the proportion of 87% (resp. 81%) for the one of Park et al. [23] (resp. Zafari et al. [18]). Moreover, there is also a good agreement in the first two moments of the distribution of the equivalent diameter.

An application of the algorithm on real images of a typical diphasic-flow encountered in chemical engineering application has highlighted the relevance of the proposed model for process monitoring purposes. Indeed, the method is automated, robust and requires a limited number of manual parameters adjustment. Typical analysis time for a classical image (1 Mpx, 200 overlapping particles) is about 2 minutes on a basic computer. Due to the sub-clustering approach, cpu time can be significantly decreased by parallelization on several cores, thus opening up perspectives for real time control and *in-situ* monitoring of multiphase flow processes. Although significant improvement is achieved thanks to the proposed algorithm, the method is still limited to systems considering simple geometric shapes (circles, ellipses, etc.). Future work will address more complex particle's shape and a direct estimation of 3D particles characteristics.

## Acknowledgment

This work was supported by the Nuclear Energy Division of CEA (program DISN/PAREC).

## References

- [1] Y. Fu, Y. Liu, Development of a robust image processing technique for bubbly flow measurement in a narrow rectangular channel, *Int. J. Multiphase Flow* 84 (2016) 217–228.
- [2] S. Maaß, A. Voigt, M. Kraume, Experimental comparison of measurement techniques for drop size distributions in liquid/liquid dispersions, *Exp. Fluids* 50 (2011) 259–269.
- [3] M. Mickler, B. Boecker, H.-J. Bart, Drop swarm analysis in dispersions with incident-light and transmitted-light illumination, *Flow Meas. Instrum.* 30 (2013) 81–89.
- [4] J. Illingworth, J. Kittler, A survey of the hough transform, *Comput. Vision Graphics Image Process.* 44 (1) (1988) 87–116.
- [5] Y. Bian, F. Dong, W. Zhang, H. Wang, C. Tan, Z. Zhang, 3d reconstruction of single rising bubble in water using digital image processing and characteristic matrix, *Particuology* 11 (2) (2013) 170–183.
- [6] Y. Xie, Q. Ji, A new efficient ellipse detection method, in: *Pattern Recognition, 2002. Proceedings. 16th International Conference on*, vol. 2, IEEE, 2002, pp. 957–960.
- [7] A. Karn, C. Ellis, R. Arndt, J. Hong, An integrative image measurement technique for dense bubbly flows with a wide size distribution, *Chem. Eng. Sci.* 122 (2015) 240–249.
- [8] O.S. Ahmad, J. Debayle, J.-C. Pinoli, A geometric-based method for recognizing overlapping polygonal-shaped and semi-transparent particles in gray tone images, *Pattern Recognit. Lett.* 32 (15) (2011) 2068–2079.
- [9] W. Kracht, X. Emery, C. Paredes, A stochastic approach for measuring bubble size distribution via image analysis, *Int. J. Miner. Process.* 121 (2013) 6–11.
- [10] Y. Lau, N. Deen, J. Kuipers, Development of an image measurement technique for size distribution in dense bubbly flows, *Chem. Eng. Sci.* 94 (2013) 20–29.
- [11] G. Bonifazi, S. Serranti, F. Volpe, R. Zucco, A combined morphological and color based approach to characterize flotation froth bubbles, in: *Intelligent Processing and Manufacturing of Materials, 1999. IPMM'99. Proceedings of the Second International Conference on*, vol. 1, IEEE, 1999, pp. 465–470.
- [12] M. Farhan, O. Yli-Harja, A. Niemistö, A novel method for splitting clumps of convex object incorporating image intensity and using rectangular window-based concavity point-pair search, *Pattern Recognit.* 46 (2013) 741–751.
- [13] C. Chow, T. Kaneko, Automatic boundary detection of the left ventricle from cineangiograms, *Comput. Biomed. Res.* 5 (4) (1972) 388–410.
- [14] A. Khalil, F. Puel, Y. Chevalier, J.-M. Galvan, A. Rivoire, J.-P. Klein, Study of droplet size distribution during an emulsification process using in situ video probe coupled with an automatic image analysis, *Chem. Eng. J.* 165 (2010) 946–957.
- [15] M. Honkanen, P. Saarenrinne, T. Stoor, J. Niinimäki, Recognition of highly overlapping ellipse-like bubble images, *Meas. Sci. Technol.* 16 (2005) 1760–1770.
- [16] W.-H. Zhang, X. Jiang, Y.-M. Liu, A method for recognizing overlapping elliptical bubbles in bubble image, *Pattern Recognit. Lett.* 33 (2012) 1543–1548.
- [17] L. Shen, X. Song, M. Iguchi, F. Yamamoto, A method for recognizing particle in overlapped particle images, *Pattern Recognit. Lett.* 21 (2000) 21–30.
- [18] S. Zafari, T. Eerola, J. Sampo, H. Kalviainen, H. Haario, Segmentation of overlapping elliptical objects in silhouette images, *Image Process. IEEE Trans.* 24 (12) (2015) 5942–5952.
- [19] H. Samet, M. Tamminen, Efficient component labeling of images of arbitrary dimension represented by linear bintrees, *IEEE Trans. Pattern Anal. Mach. Intell.* 10 (4) (1988) 579–586.
- [20] F. Pla, Recognition of partial circular shapes from segmented contours, *Comput. Vision Image Understanding* 63 (2) (1996) 334–343.
- [21] M. Altheimer, R. Häfeli, C. Wälchli, P.R. von Rohr, Shadow imaging in bubbly gas-liquid two-phase flow in porous structures, *Exp. Fluids* 56 (9) (2015) 177.
- [22] A. Fitzgibbon, M. Pilu, R.B. Fisher, Direct least square fitting of ellipses, *IEEE Trans. Pattern Anal. Mach. Intell.* 21 (1999) 476–480.
- [23] C. Park, J.Z. Huang, J.X. Ji, Y. Ding, Segmentation, inference and classification of partially overlapping nanoparticles, *IEEE Trans. Pattern Anal. Mach. Intell.* 35 (3) (2013) 669–681.
- [24] S. Zafari, T. Eerola, J. Sampo, H. Kalviainen, H. Haario, Segmentation of partially overlapping nanoparticles using concave points, in: *International Symposium on Visual Computing*, Springer, 2015, pp. 187–197.
- [25] R. Clift, J.R. Grace, M.E. Weber, *Bubbles, Drops, and Particles*, Courier Corporation, 2005.
- [26] N. Otsu, A threshold selection method from gray-level histograms, *IEEE Trans. Syst. Man Cybern.* 9 (1) (1979) 62–66.
- [27] B. Presles, J. Debayle, G. Févotte, J.-C. Pinoli, Novel image analysis method for in situ monitoring the particle size distribution of batch crystallization processes, *J. Electron. Imaging* 19 (3) (2010). 031207–031207.
- [28] M. Riaz, S. Park, M.B. Ahmad, W. Rasheed, J. Park, Generalized laplacian as focus measure, in: *International Conference on Computational Science*, Springer, 2008, pp. 1013–1021.
- [29] A. Baddeley, E.B.V. Jensen, *Stereology for Statisticians*, CRC Press, 2004.
- [30] R. Miles, Estimating aggregate and overall characteristics from thick sections by transmission microscopy, *J. Microsc.* 107 (3) (1976) 227–233.
- [31] H. Gundersen, Estimators of the number of objects per area unbiased by edge effects, *Microsc. Acta* 81 (2) (1978) 107–117.